



HAL
open science

Investigation of the thermal conductivity enhancement mechanism of polymer composites with carbon-based fillers by scanning thermal microscopy

Wenxiang Sun, Georges Hamaoui, Matej Micusik, Tuba Evgin, Anna Vykydalova, Maria Omastova, Séverine Gomés

► To cite this version:

Wenxiang Sun, Georges Hamaoui, Matej Micusik, Tuba Evgin, Anna Vykydalova, et al.. Investigation of the thermal conductivity enhancement mechanism of polymer composites with carbon-based fillers by scanning thermal microscopy. *AIP Advances*, 2022, 12 (10), pp.105303. 10.1063/5.0099755 . hal-03799458

HAL Id: hal-03799458

<https://hal.science/hal-03799458v1>

Submitted on 5 Oct 2022

HAL is a multi-disciplinary open access archive for the deposit and dissemination of scientific research documents, whether they are published or not. The documents may come from teaching and research institutions in France or abroad, or from public or private research centers.

L'archive ouverte pluridisciplinaire **HAL**, est destinée au dépôt et à la diffusion de documents scientifiques de niveau recherche, publiés ou non, émanant des établissements d'enseignement et de recherche français ou étrangers, des laboratoires publics ou privés.

Investigation of the thermal conductivity enhancement mechanism of polymer composites with carbon-based fillers by scanning thermal microscopy

Authors and affiliation

Wenxiang Sun¹, Georges Hamaoui², Matej Micusik³, Tuba Evgin⁴, Anna Vykydalova³, Maria Omastova³ and Séverine Gomés^{1*}

¹Centre d'Energétique et de Thermique de Lyon (CETHIL), UMR CNRS 5008, INSA Lyon, UCBL, Université de Lyon, Villeurbanne, France

²Univ Gustave Eiffel, CNRS, ESYCOM, 2 Bd Blaise Pascal, F -93160 Noisy-le-Grand, France

³Polymer Institute, SAS, Dúbravská cesta 9, 845 41 Bratislava, Slovak Republic

⁴Dokuz Eylul University, Engineering Faculty, Mechanical Engineering Department, Tinaztepe Campus, 35397, Buca, Izmir, Turkey

Abstract

In order to elucidate the mechanism of enhancement of heat transfer in polymer composites, in this work, we investigated two types of polymer-carbon filler composite. This investigation was made using scanning thermal microscopy (SThM) using the Wollaston microprobe operated in active mode as a function of the carbon filler weight fraction within the polymer matrix. Samples consist of high-density polyethylene (HDPE) filled with 50 μm expanded graphite (EG) and polyvinylidene difluoride (PVDF) containing multiwall carbon nanotubes (MWCNTs). For HDPE/EG samples SThM images allow the detection of zones with a thermal conductance larger than that of the matrix for the highest studied filler's concentration. These zones correspond to EG filler agglomerations within the polymer and explain the observed enhancement of the thermal conductivity k of the HDPE/EG composite. For PVDF/MWCNTs samples it is found from that k increases from 0.25 $\text{W}\cdot\text{m}^{-1}\cdot\text{K}^{-1}$ for pristine PVDF to 0.37 $\text{W}\cdot\text{m}^{-1}\cdot\text{K}^{-1}$ for PVDF nanocomposites filled with 8 wt.% MWCNTs. This k variation versus filler concentration is found in good correspondence with that of the β phase relative percentage in the PVDF nanocomposites. This suggests that the observed heat transfer enhancement is rather due to the formation of β phase for PVDF/MWCNTs samples resulting of the addition of MWCNTs than the addition of MWCNTs itself. Thus, tuning the thermophysical properties of polymer-based nanocomposites can establish new design laws to confer them specific thermal properties.

*Corresponding author: severine.gomes@insa-lyon.fr

1. Introduction

Polymer-based materials have been considered as one of the materials with most development prospects and application market, because of low cost, excellent processability, light weight, and excellent flexibility. Polymers are in great demand in various industrial fields such as the electrical industry, fuel cells, the packaging industry and architectural engineering, etc. In recent years, with the booming development of microelectronic devices industry, the requirement for enhanced heat dissipation components began to arise. However, due to continual scattering of energy carriers, for most polymer the thermal conductivity (k) is low, in the range of 0.1 to 0.5 W.m⁻¹.K⁻¹. In this case, improving the k of polymers-based systems have become a very active research topic ^{2,3}.

The insertion of fillers such as ceramics materials ^{4,5}, metallic materials ⁶⁻⁹ and carbon-based materials ¹⁰⁻¹² is a popular strategy to enhance the thermal conductivity of polymer composites. Among all these fillers, carbon-based materials have aroused higher attention and interest of scholars due to their thermophysical properties exhibiting a thermal conductivity that can even reach values higher than several thousands of W.m⁻¹.K⁻¹ for fillers such as carbon fibers and carbon nanotubes in their axial direction ¹³. For such reasons, a large number of studies have been carried out to improve the polymer k using carbon-based nano-fillers ^{10-12,14-17}. For example, Chirtoc et al. ¹⁶ have introduced expanded graphite (EG) fillers into high-density polyethylene (HDPE) and achieved increased thermal conductivity when the filler concentration increases in the range up to 0.06 graphite volume fraction. However, it was recognized from this study that the experimental results obtained using a modulated

photothermal radiometry (PTR) method deviate from those predicted by the model of Nan et al.¹⁸ for filler at higher concentrations¹⁶. A proposed reason was that the non-interacting particle assumption of the model is not valid as the filler concentration increases.

Furthermore, in addition to HDPE, several other types of polymers are widely employed as base matrix for nanocomposites, like polyvinylidene fluoride (PVDF), due to their excellent film formation, mechanical properties, high resistance towards chemicals, alongside a thermal, oxidative, and hydrolytic stability^{19,20}. Specifically, Georgousis et al.¹⁷ have dispersed multiwall carbon nanotubes (MWCNTs) in PVDF and observed that the electrical and mechanical properties of the PVDF matrix improve after adding the MWCNTs, which give an advantage of such polymer for prospective strain sensing applications. However, the effect of introducing MWCNTs on the thermal properties of these PVDF – based composites is still missing. The characterization of the thermophysical properties of the combination PVDF/MWCNTs would be favorable to supplement the understanding of the influence produced by MWCNTs on the polymer matrix and to suggest other applications of the material.

Various thermal conductivity measurement techniques have already been used to characterize polymer-based composites, including electrical-based ones such as the 3ω method²¹, scanning thermal microscopy (SThM)²², and optical methods such as flash method²³, photothermal radiometry (PTR) technique¹⁶ and thermoreflectance²⁴. Specifically, the optical methods generally require the deposition of an optical transducer layer on the film's surface in order to induce a surface heat absorption of the optical energy. Moreover, contact techniques, such as the 3ω method, involve the deposition of metallic contacts resistances on the samples'

surface to induce a Joule effect. Hence, some characterization techniques can damage the studied materials and are considered as destructive methods. However, by using a microprobe, SThM can be an approach for thermal conductivity measurements allowing the thermal investigation of several μm^3 subsurface volumes in polymeric materials without any preliminary processing of the sample's surface²⁵. Therefore, we used the SThM technique to perform thermal analysis in this work.

The SThM method, originating from the scanning probe microscopy (SPM) method, is mainly based on the atomic force microscopy (AFM) technique equipped with a small thermoresistive probe. In the frame of thermal property characterization, so called active mode, the probe is self-heated by Joule effect, and is used simultaneously as a local heating source and a resistive thermometer. The capability and feasibility for SThM to be applied to polymeric materials have been demonstrated by prior researches^{26–28} but previous thermophysical analyses have mainly been qualitative^{26,27} or have instead concerned ultra-localized calorimetry measurements^{28,29}. The SThM capability to perform thermal conductance images and to detect local thermal conductivity inhomogeneities and distributions²⁵ have indeed been demonstrated. It could provide more information to more deeply understand the heat transport enhancement mechanisms in polymer nanocomposites. Consequently, a methodology to estimate the effective thermal conductivity of polymer nanocomposites is required.

Hence, in order to verify the thermal conductivity results obtained by Chirtoc et al.¹⁶, and to obtain the complementary thermal conductivities for the samples of Georgousis et al.¹⁷, we will first give a comprehensive methodology developed to measure the effective thermal

conductivity of polymer composites using SThM and will carry out additional measurements on the same sample types with this methodology. We will experimentally characterize heat transport in such polymer-carbon filler composites (HDPE/EG¹⁶ and PVDF/MWCNTs¹⁷) by means of SThM not only to measure the effective thermal conductivity (k_{eff}) but also to investigate the mechanisms of enhancement of heat transfer. The SThM technique will allow us to investigate the local thermophysical properties of polymeric materials with a micrometric spatial resolution, providing some possibilities to demonstrate any agglomeration effects. The result of this study may provide a new point of view for the management and tuning of thermophysical properties of polymer-based composite.

2. Experimental

2.1 Materials

High density polyethylene (HDPE) BP 5740 3 VA, supplied by British Petroleum UK, was used as matrix. Expanded graphite, particle sizes of 50 μm (EG50), Ecophit G, supplied by SGL Technologies GmbH. The PVDF (SOLEF1010, Solvay Solexis S.A., Belgium) was supplied in the form of pellets. The MWCNTs (Nanocyl7000, Belgium; purity of 90%, outer diameter of 9.5 nm and length 1.5 μm) were used as received.

2.2 Sample description

2.2.1 HDPE/EG composites

HDPE was filled with 2 % and 10 % weight fraction (wt.%) of 50 μm EG in a Brabender Plasticorder PLE 331 apparatus as described in¹⁶. The thickness of samples after compression

molding was around 0.3 mm. Optical observation suggests that large EG flakes were broken during preparation process and formed smaller fragments with observed size less than 10 μm ¹⁶.

2.2.2 PVDF/MWCNTs composites

PVDF matrix with MWCNT fillers of an outer diameter of 9.5 nm and length 1.5 μm were prepared by melt mixing in a microcompounder DSM Xplore TM 15 (the Netherlands) using the parameters detailed in¹⁷. Composites containing 0.5, 1, 1.25, 1.5, 1.75, 2, 3, 4, 6, 8 wt.% MWCNTs have been studied. The thickness of PVDF/MWCNTs samples was around 0.5 mm.

The morphology was studied using scanning electron microscopy (SEM) and no large agglomeration of MWCNTs is observed.

Infra-red spectra (FTIR) of pure PVDF and PVDF/MWCNTs nanocomposite films were acquired with NICOLETE 8700 (Thermo Scientific, Madison USA) in Micro-ATR mode, with resolution 4 cm^{-1} , 320 scans, in the range between 4000 and 650 cm^{-1} . The differential scanning calorimetry (DSC) measurements were performed on DSC 821 Mettler Toledo (Mettler-Toledo, Greifensee, Switzerland). Samples were placed in aluminum pan with lid and the weight of them were 3.5 - 4 mg. As a purge gas was used nitrogen with 50 mlmin^{-1} flow. The samples were heated from 0 to 200 $^{\circ}\text{C}$ at 5 $^{\circ}\text{Cmin}^{-1}$, then held for 2 min at this temperature, cooled to 0 $^{\circ}\text{C}$ at same heating rate and again heated to 200 $^{\circ}\text{C}$. The total crystallinity of PVDF materials was calculated by using the equation: $\chi_c = \frac{\Delta H_m}{\Delta H_m^c} \times 100\%$, where ΔH_m is the melting enthalpy of the sample and ΔH_m^c is the melting enthalpy with a value of 104.7 Jg^{-1} for crystalline PVDF

³⁰.

2.3 Experimental setup

The experiments were performed in ambient air environment using a NTEGRA-Aura AFM (NT-MDT, Russia) equipped with a SThM module allowing imaging the topography of the sample and the thermal conductance of a sample subsurface simultaneously. The SThM probe used in these works is the Wollaston wire probe³¹ (Fig 1). This probe consists of a 5 μm diameter rhodium-plated (10 %) platinum filament (90 %) (Pt/Rh) core and a 35 μm silver shell. The resistive element at the end of the tip is obtained by electrochemical etching of the silver shell, allowing stripping a 200 μm segment rhodium-plated platinum filament core previously bended into a V-shape. A mirror is glued on the cantilever to reflect the laser toward the AFM photodetector that allows measuring the force between the probe and the sample. We used this probe in active mode and dc regime, and assumed that, due to its relatively high electrical resistance compared to that of the silver shell, only the uncovered Pt/Rh wire generates heat by Joule effect within the probe. A linear relationship between the variation of electrical resistance and the mean probe temperature rise ΔT with respect to ambient temperature T_a can be applied to the Pt/Rh resistive element:

$$\Delta R_{el,Pt} = R_0 \Delta T \alpha_0 \quad (1)$$

where $\Delta R_{el,Pt}$ represents the variation of the electrical resistance of the resistive element as a function of its mean temperature (\bar{T}_{Pt}); R_0 is the electrical resistance at T_a ; $\Delta T = \bar{T}_{Pt} - T_a$; and α_0 is the temperature coefficient of electrical resistance (TCR) of the resistive element at T_a . Meanwhile, a balanced Wheatstone bridge was used to maintain constant the total electrical resistance of the probe $R_{el,p}$ ($\Delta R_{el,Pt} = 0$) and then to maintain constant the probe mean

temperature.

Fig 1. Optical image of a Wollaston probe.

Measurements were made in two steps. First the voltage of the probe U_{oc} is measured while the probe is out of contact with the sample and at a distance of the sample surface of 2 mm. Second the probe is in contact with the sample and topography and thermal images were performed. The value of the probe's voltage averaged on the scanned surface (in contact) is denoted U_{ic} . Knowing the electrical resistance of all the components in the Wheatstone bridge, the currents passing through the resistive element I_{oc} and I_{ic} can be derived from U_{oc} and U_{ic} , respectively. One should note that throughout the manuscript the subscripts oc and ic denote the two steps of the measurements, out of contact and in contact, respectively.

2.4 Measurement modeling and calibration

The voltage difference $U_{ic} - U_{oc}$ represent the variation of the thermal conductance of the probe G between out of contact (G_{oc}) and in contact (G_{ic}) configurations:

$$G_{ic} - G_{oc} = \frac{P_{Pt-ic} - P_{Pt-oc}}{\Delta T} \quad (2)$$

where $P_{Pt-ic} = R_{Pt}I_{ic}^2$ and $P_{Pt-oc} = R_{Pt}I_{oc}^2$ are the electrical power dissipated in the resistive element while the probe is out of contact and in contact with sample, respectively. The temperature at the apex of the Pt/Rh tip has been proved to be around 1.5 time of the mean temperature of the resistive wire³². However, it is very difficult to determine experimentally the tip apex part and its dimension. Furthermore, when not in vacuum, the thermal contact area

is not just limited in the apex part due to heat conduction through the gas³². Therefore, we consider in eq. 2 that the whole Pt/Rh wire is isothermal and that the mean temperature \bar{T}_{Pt} was used to calculate the thermal conductances G_{oc} and G_{ic} .

As represented in Fig 2, which gives the thermal conductance network of the probe out of contact with a sample, G_{oc} can be written as:

$$G_{oc} = G_{env} + G_{wire} \quad (3)$$

where G_{env} corresponds to the heat dissipated to the environment by convection (radiation effect is small enough to be neglected³²) and G_{wire} corresponds to the heat conduction to the probe cantilever in Wollaston wire.

When the probe comes into contact with the surface of the sample, G_{ic} can be expressed as:

$$G_{ic} = G_s + G'_{env} + G_{wire} \quad (4)$$

G_{env} changes to G'_{env} due to the shielding effect of the sample from heat exchange between the tip and environment²². In addition, a new heat transfer channel towards the sample G_s arises. G_s can be expressed as³²:

$$G_s = \frac{G_{ss}G_c}{G_{ss} + G_c} \quad (5)$$

where G_c is the thermal conductance corresponding to the heat transfer between the probe and the sample through solid-solid contacts, water meniscus and the gas, and G_{ss} is the thermal conductance of the sample. In the case of diffusive samples, G_{ss} can be expressed as³²:

$$G_{ss} = 4k_{eff}a \quad (6)$$

where a is the effective radius of the thermal contact assumed discoidal (as exposed in Fig 2).

Fig 2. Representation of the heat transfers within the SThM probe while out of contact (a) and in contact (b) and the associated thermal resistance network.

Then the following equation can be obtained by combining eq. 2 to eq. 6,

$$G_{ic} - G_{oc} = G_s + G'_{env} - G_{env} = \frac{G_c}{1 + \frac{G_c}{4k_{eff}a}} + G'_{env} - G_{env} \quad (7)$$

$$P_{ic} - P_{oc} = \frac{G_c \Delta T}{1 + \frac{G_c}{4k_{eff}a}} + (G'_{env} - G_{env}) \Delta T \quad (8)$$

ΔT is a constant. With the assumption that a and G_c are invariable with k_{eff} ^{33–36}. We may plot $P_{ic} - P_{oc}$ in a curve with the shape $P_{ic} - P_{oc} = \frac{A}{1 + \frac{B}{k_{eff}}} + C$, which can be used in the probe calibration for thermal conductivity measurements³².

Fig 3 gives the calibration curve experimentally obtained using our SThM with a series of bulk reference samples with well-known thermal conductivity in the range 0.187-1.28 W.m⁻¹.K⁻¹ and well-known roughness (lower than 15 nm)³⁷. The good fitting of experimental data using the above formula is demonstrated. The corresponding curve was used to find the effective thermal conductivity of the studied samples (k_{eff}).

Fig 3. Calibration curve obtained experimentally from the measurement of reference samples³⁷: PMMA ($k_{PMMA} = 0.187 \text{ W. m}^{-1} \cdot \text{K}^{-1}$), POM-C ($k_{POM-C} = 0.329 \text{ W. m}^{-1} \cdot \text{K}^{-1}$), Glass ($k_{Glass} = 1.11 \text{ W. m}^{-1} \cdot \text{K}^{-1}$) and SiO₂ ($k_{SiO_2} = 1.28 \text{ W. m}^{-1} \cdot \text{K}^{-1}$). The equation in red is the expression of the fitting curve of the measurements.

2.5 Measurement method

The samples from the same series were cut into small pieces and glued on same sample holder to avoid changing the environment around the SThM probe when changing the sample.

Systematical topography analysis is important for properly interpreting the SThM measurements. On one hand, a and G_c strongly depend on mechanical contact between the probe and the sample surface, which is affected by the roughness³⁸. In order to make the hypothesis that a and G_c are constant as valid as possible, the selected area with a flat surface is preferable for measuring accurately the thermophysical properties of the samples without topography artifact. On the other hand, it has been well demonstrated in literature that the heat dissipation towards polymer samples strongly depends on the contact area and the air gap between probe and sample³⁹⁻⁴¹. To avoid the artificial thermal signal variation induced by such effects in our measurements, the thermal and topography images of polymer composite samples were performed simultaneously with the same Wollaston probe at scanning frequencies of 0.1-0.4 Hz, which ensures that the scan time for each pixel is much larger than the thermal response time of the probe (1 ms). The scan was performed on an area of $100 \mu\text{m}^2$ initially to obtain the overall information of sample surface. For the samples that show a mismatch between the topography and the thermal image, additional investigation was performed on the interested zone using a smaller scan area size, allowing to avoid topography artifact in the thermal signal. To study the thermal conductivity of a specific area, an average value of U_{ic} for a square containing at least 25 pixels was recorded. For the case of the samples with homogeneous k_{eff} distribution, five of such squares with low roughness were selected and taken into average.

3. Results and discussion

The effective thermal conductivity of the two studied material sets (see section 2.2) were measured applying the methodology previously described.

3.1 Measurement results for HDPE/EG composites

Fig 4. SThM images for HDPE composite containing 2 % (a, b) and 10 % (c, d) weight fractions of EG. Topography (a, c) and thermal) signal (b, d).

Fig 4 displays the topography and thermal images obtained simultaneously of HDPE composites filled with 2 and 10 wt.% of EG, respectively. Benefit from the synchronization of morphology and thermal signal acquisition, it is possible to analyze these data from the exact same region. The topography (Fig 4a) and thermal (Fig 4b) images of 2 wt.% EG contained in a HDPE matrix present a high degree of consistency in contrast, which means the variation of heat loss flux is due to the topography features of the sample surface. The bright part indicating higher heights may be caused by the dust or surface defect formed during the fabrication. By averaging the thermal signal from the flat part on the thermal image, $k_{eff} = 0.45 \pm 0.02 \text{ W.m}^{-1}.\text{K}^{-1}$ was determined by using the calibration curve shown in Fig 3. The uncertainty is calculated from the root mean square of U_{ic} . The identified k_{eff} value is lower than the result (0.59 $\text{W.m}^{-1}.\text{K}^{-1}$) measured on the same sample with back-detection PTR method but close to the result $\sim 0.40 \text{ W.m}^{-1}.\text{K}^{-1}$ for neat HDPE (pristine, without any fillers)¹⁶. The reason of the lower value from SThM measurements may come from the lack of EG fillers contained in limited probed

volume, what is expected for a composite with low filler concentration such as 2 wt.%.

This result proves the reliable sensitivity of SThM in the studied thermal conductivity range. The deviation of the results obtained by SThM and PTR techniques verifies the inhomogeneity of dispersion of EG fillers at low concentration. In ref. ¹⁶, it has been shown that the experimental result from back-detection PTR method fit well with the effective thermal conductivity of composite model of Nan et al. ¹⁸ when filler charge is less than 6 vol.%. It is worth to note that this model is effective with the assumption regarding non-interacting fillers. No agglomeration of EG observed from SThM is also favorable to the validation of this assumption.

On the contrary to 2 wt.% EG fraction sample, HDPE composite with 10 wt.% filler charge shows a different contrast pattern between thermal and topography images as circled in Fig 4c (zones A and B). The dark area in thermal image indicates a higher heat transfer from the probe to the sample that corresponds to a higher local thermal conductance of the sample. Meanwhile, the same position on topography image has a shallower color associated with higher heights.

Furthermore, as explained above, the topography of the sample surface may induce some artifacts in the thermal images. This can be linked to the fact that the contact radius may reach more than 5 μm for Wollaston probe on polymeric materials ⁴², which is comparable to the size of convex zones for the sample. The scanning of the SThM probe on a concave surface may induce more thermal exchange due to the increase of contact area through the air gap, which does not agree with our results. Therefore, the thermal signal contrast obtained can only be attributed to the variation of the thermal properties beneath the surface of sample. Besides, these

high thermal conductance regions are distributed as islands inside the sample. The agglomerations of EG fillers are supposed to be the reason behind this phenomenon.

Fig 5. Effective thermal conductivity of HDPE/EG composite with 10 wt.% filler charge measured at different locations that are precised in Fig 4 (c). The root mean square was considered as the uncertainty and used to estimate the error bar.

After comparing the topography and the thermal images of the samples, the second step of the measurement was to identify k_{eff} of the polymeric-based nanocomposites. Eight locations were chosen randomly as indicated in Fig 4c, and the thermal conductivity was calculated using the averaged signal at each location. Results are given in Fig 5. As shown in Fig 5, all the results fall within the range from 0.67 to 1.06 $\text{W}\cdot\text{m}^{-1}\cdot\text{K}^{-1}$, which is close but still lower than the k_{eff} values measured by other methods (1.27 $\text{W}\cdot\text{m}^{-1}\cdot\text{K}^{-1}$ for PTR¹⁶, 1.26 $\text{W}\cdot\text{m}^{-1}\cdot\text{K}^{-1}$ for Flash method⁴³ and 1.23 $\text{W}\cdot\text{m}^{-1}\cdot\text{K}^{-1}$ from modelling¹⁶). The reason that the SThM results are lower compared to the other techniques could also be linked to the lack of fillers contained in the limited probed volume of the sample. One should keep in mind that the SThM area for investigation was $100 \times 100 \mu\text{m}$, and the original EG particles size was $50 \mu\text{m}$, which was broken during preparation to smaller fragments with size less than $10 \mu\text{m}$. This fact can also contribute to inhomogeneity of measured value of thermal conductivity. Nonetheless, the enhancement of the heat transfer along higher concentration of EG fillers can be clearly demonstrated by SThM, comparably to other techniques.

Fig 6. Topography image (a) and thermal image (b) of 10 % weight fraction of EG-HDPE sample. (c) and (d): associated histograms giving the distribution of the height and thermal signal values respectively.

To further investigate and demonstrate our conjecture, the same scanning procedure was performed on another zone of the sample 90HDPE-10EG with $50\mu\text{m}\times 50\mu\text{m}$ area size. The mismatch of the topography and thermal contrast also appears clearly on these images as shown in Fig 6. The distribution curve of the signals is also represented in this figure. The distribution curve for the height of the sample presents only one peak, demonstrating that the surface is flat. Two peaks appear on the thermal signal distribution curve, indicating the existence of two levels of thermal conductance within the sample. These peaks cannot be correlated to the topography of the sample surface.

We can observe in the top right corner of Fig 6b a dark area where the sample thermal conductance is larger than elsewhere at the surface. This kind of relatively high thermal dissipation area with such large size only arises while the weight fraction of EG reaches 10 %. The estimated diameter of this area, which is around $20\mu\text{m}$ from thermal image, is larger than EG intercalation diameter $5\text{-}10\mu\text{m}$ that is observed under optical microscope for HDPE98-EG2 sample¹⁶. The possible reason of the formation of large heat sink area may be related to the agglomeration due to Van der Waals interaction between graphene platelets⁴⁴ of the EG with a high specific surface area⁴⁵⁻⁴⁷.

All these results further prove the capability of SThM to detect the local thermal conductivity variation among different zones of the polymer composites, which is arisen by the fillers buried beneath the surface.

3.2 Measurement results for PVDF/MWCNTs samples

Due to the rather high roughness on the surface of PVDF/MWCNTs samples, the contrast in thermal images is almost identical with the topography image. Fig 7 shows the topography and thermal images for composite containing 4 wt.% MWCNTs as an example. No obvious difference can be observed from the two images, that is in good agreement with the well dispersion of MWCNTs inside the PVDF matrix proved by SEM images¹⁷.

Fig 7. Topography and thermal images for the PVDF composite containing 4 wt.% MWCNTs.

The k_{eff} of the samples is calculated from the average value of the signal lying inside selected area that avoids the variation caused by roughness as much as possible. The results have been plotted as a function of MWCNTs weight fraction in Fig 8. It can be seen that an enhancement of thermal conductivity is achieved with the addition of MWCNTs. No percolation behavior, as detected for electrical conductivity¹⁷, appears in the thermal properties, in agreement with the results reported in literature⁴⁸. The reason may be that the expansion of heat flux aroused by the formation of MWCNTs network is very slight due to relatively small thermal conductivity ratio between MWCNTs and PVDF matrix compared to electrical issue. The heat dissipated through polymer matrix is still the main part of heat transfer⁴⁹. Another possibility is the high thermal resistance at the interface between individual carbon nanotube, leading to the insufficient channel for heat transfer⁵⁰. The k_{eff} reaches $0.37 \text{ W}\cdot\text{m}^{-1}\cdot\text{K}^{-1}$ while the fillers loading is 8 wt.%, which is at the same level compared to PVDF filled with graphene ($0.32 \text{ W}\cdot\text{m}^{-1}\cdot\text{K}^{-1}$ for 10 wt.%)⁵¹ or conducting carbon black ($0.4 \text{ W}\cdot\text{m}^{-1}\cdot\text{K}^{-1}$ for 10 wt.%)⁵², but

lower than the one filled with reduced graphene oxide (rGO) ($0.89 \text{ W}\cdot\text{m}^{-1}\cdot\text{K}^{-1}$ for 3 wt.%)⁵³. The dependence of crystallites size on filler concentration is proposed to explain the enhancement of thermal conductivity⁵³. It is worth to note that in our measurement, the trend of the thermal conductivity results is in concurrence with the PVDF β and γ phase relative percentage versus MWCNTs weight fraction.

PVDF exhibits five crystalline phases (α , β , γ , δ and ϵ) due to the arrangement of $-\text{C}(\text{F})-$ dipoles. Antiparallel composition of α and ϵ results in non-polar PVDF. The next three phases are polar and show piezoelectric and ferroelectric properties⁵⁴. The most electroactive phases are β and γ ⁵⁵. FTIR spectra are showing many overlapping peaks of α , β and γ phases, but some of them are unique for certain phase and can be used for identification and quantification⁵⁶. FTIR spectra in Fig 9a shows these characteristic peaks for α phase (763 cm^{-1}), β phase (840 cm^{-1}) and γ phase (1231 cm^{-1}). To properly distinguish these three phases also other techniques are recommended. One of the possible techniques is DSC measurements and evaluation of melting temperatures of various crystallites. The melting temperature of α and β crystallites are very similar at $167\text{-}171^\circ\text{C}$, but γ crystallites melt at slightly higher temperature at $175\text{-}180^\circ\text{C}$ ^{57,58}. DSC shown in Fig 9b confirms the presence of γ crystallites melted at slightly higher temperature of 176°C than α and β crystallites (T_m at 171°C). The addition of MWCNTs showing the slight decreasing trend in crystallinity of samples (PVDF $64.5\% > 3\text{wt.}\% 59.1\% > 8\text{wt.}\% 57.7\%$). Also the same trend can be seen in enthalpies of melting ($67.6 > 61.9 > 60.4 \text{ Jg}^{-1}$). The addition of MWCNTs has no influence on crystallization temperature which is at 150°C . The separation of two visible peaks in Fig 9b is difficult because of their very close distance. We can only assume their percentage in melting peaks. Used some mathematic, we can assume

that the percentage of the γ phase in sample containing 3wt.% of MWCNTs is ~9% and the percentage in sample with 8wt.% of MWCNTs is ~12.5%. The increasing effect of MWCNTs is also visible in Fig 9b where can be seen the growing of peaks corresponding to the γ phase.

The β phase PVDF is a kind of crystalline polar polymer with an all-trans conformation, which is suggested to be favorable for the heat transfer by increasing the mean free path of energy carriers⁵⁹. The γ phase PVDF has significantly lower dipole moment than that of the β phase⁶⁰. Consequently, it is reasonable to suppose that the formation of β and γ phase PVDF may facilitate the thermal transport considering that the electric and thermal current flows at macroscopic dimension share the same equation⁴⁹. The β phase PVDF contribution thanks to higher polarity and crystallinity percentage will be more pronounced than the contribution of γ phase. In summary, the formation of MWCNTs heat conduction paths and a relatively higher crystallinity of PVDF matrix lead to the enhancement of the composite k_{eff} .

Fig 8. Thermal conductivity and β phase relative percentage of PVDF/MWCNTs composite versus weight fraction % of MWCNTs). Solid lines are not fitting curves but guide for eyes to compare the tendency of data.

Fig 9. a) FTIR of pure PVDF and PVDF composites with 4 and 8 wt.% of MWCNTs; b) DSC of pure PVDF and PVDF composites with 3 and 8 wt.% of MWCNTs.

4. Conclusion and perspectives

We investigate through SThM measurements the heat transfer enhancement mechanisms in two types of polymer-carbon filler composite i) HDPE filled with 50 μm EG composites and ii) PVDF/MWCNTs composites, versus carbon filler weight fraction within the polymer. In principle, the characterization of the thermal conductivity of polymer composites phenomena, such as agglomeration effect, can only be suggested from the combination of effective modeling with measurements at the macroscale. To this end, in this manuscript we proved that the SThM technique allows the local investigation of polymeric materials with a micrometric spatial resolution, providing some possibilities to demonstrate the aforementioned agglomeration effect.

For HDPE/EG samples SThM images allow the detection of zones with a thermal conductance larger than that of the matrix for the highest filler concentration studied. These zones correspond to EG filler agglomerates within the polymer and explain the observed enhancement of the thermal conductivity of the HDPE/EG composite. The k_{eff} results obtained by SThM are comparable but lower than those measured by PTR method, flash method and modeling. The reason may be that the inhomogeneous distribution of EG fillers can affect the representativeness of data collected by microscale probe. In this case, the k_{eff} account more heat transfer capability of polymer matrix than the real situation. This has been well demonstrated by the result of HDPE/EG composite with 2 wt.% fillers.

For PVDF/MWCNTs samples it is found from that thermal conductivity increases from 0.25 $\text{W}\cdot\text{m}^{-1}\cdot\text{K}^{-1}$ for pristine PVDF to 0.37 $\text{W}\cdot\text{m}^{-1}\cdot\text{K}^{-1}$ for PVDF nanocomposites filled with 8 wt.%

MWCNTs. This variation versus filler concentration is found in good correspondence with that of the β phase relative percentage in the PVDF nanocomposites. This suggests that the observed heat transfer enhancement is rather due to the formation of β phase for PVDF/MWCNTs samples resulting of the addition of MWCNTs than the addition of MWCNTs itself. MWCNTs disperse well and form heat conduction network in the PVDF. MWCNTs can also promote the formation of β and γ phase crystallites, which increase the mean free path of energy carries and then the thermal conductivity of samples.

Such thermally conductive polymer composites can help solving the current heat dissipation issues in different applications, using polymer-based material, like in automobile, packaging, aerospace, energy harvesting, electromagnetic interfaces (EMIs), fifth-generation mobile network, and electronic devices industries. The result of this study may provide a new point of view for the management and tuning of thermophysical properties of polymer-based composite.

Perspectives of this work include the application of the SThM technique to other polymer composites with carbon-based nanofillers such as graphene or rGO nanosheets for comparison and innovative 2D material nanoflakes. Additionally, a theoretical model is under development to go deeper in the understanding of the impact of the β phase of PVDF on heat transport in PVDF/MWCNTs materials.

Author Contributions:

Wenxiang Sun: Investigation, Data Curation, Writing-original draft, Writing-review & editing.

Georges Hamaoui: Supervision, Writing-original draft, Writing-review & editing.

Matej Micusik: Resources, Investigation, Data Curation, Writing-original draft.

Tuba Evgin: Resources, Writing-review & editing

Anna Vykydalova: Investigation, Data Curation, Writing-original draft.

Maria Omastova: Resources, Writing-review & editing

S everine Gom es: Supervision, Writing-original draft, Writing-review & editing, Project administration.

Declaration of competing interest: The authors declare that they have no known competing financial interests or personal relationships that could have appeared to influence the work reported in this paper.

Acknowledgments: W. S, G. H. and S. G. acknowledge support of project TIPTOP (ANR-16-CE09-0023) and the China Scholarship Council (CSC). This work was partially supported by Slovak Grant Agency, projects No. APVV-SK-BY-RD-19-0011, and VEGA: 2/00006/22.

Data Availability Statement: The data that support the findings of this study are available from the corresponding author upon reasonable request.

5. Reference

- ¹ X. Huang, P. Jiang, and T. Tanaka, IEEE Electrical Insulation Magazine **27**, 8 (2011).
- ² X. Xu, J. Zhou, and J. Chen, Adv Funct Mater **30**, (2020).
- ³ H. Ma, B. Gao, M. Wang, Z. Yuan, J. Shen, J. Zhao, and Y. Feng, J Mater Sci **56**, 1064 (2021).
- ⁴ C.Y. Kim, T.M. Linh Dang, Y. Zhang, J.F. Yang, and B. Wang, Journal of Materiomics **5**, 679 (2019).
- ⁵ J. He, H. Wang, Z. Su, Y. Guo, Q. Qu, T. Qin, and X. Tian, ACS Appl Polym Mater **1**, 2807 (2019).
- ⁶ S. Chung, Y. Im, H. Kim, S. Park, and H. Jeong, J Mater Process Technol **160**, 168 (2005).
- ⁷ H.M. Ragab and A. Rajeh, Journal of Materials Science: Materials in Electronics **31**, 16780 (2020).
- ⁸ S. Yu, J.W. Lee, T.H. Han, C. Park, Y. Kwon, S.M. Hong, and C.M. Koo, ACS Appl Mater Interfaces **5**, 11618 (2013).
- ⁹ T. Giang, J. Park, I. Cho, Y. Ko, and J. Kim, Polym Compos **34**, 468 (2013).
- ¹⁰ E.M. Jackson, P.E. Laibinis, W.E. Collins, A. Ueda, C.D. Wingard, and B. Penn, Compos B Eng **89**, 362 (2016).
- ¹¹ S.Y. Yang, W.N. Lin, Y.L. Huang, H.W. Tien, J.Y. Wang, C.C.M. Ma, S.M. Li, and Y.S. Wang, Carbon N Y **49**, 793 (2011).
- ¹² Y.S. Jun, J.G. Um, G. Jiang, G. Lui, and A. Yu, Compos B Eng **133**, 218 (2018).
- ¹³ Z. Han and A. Fina, Progress in

- Polymer Science (Oxford) **36**, 914 (2011).
- ¹⁴ Y. Zhang and S.J. Park, Polymer (Guildf) **168**, 53 (2019).
- ¹⁵ H. Ye, B. Han, H. Chen, and L. Xu, Nanotechnology **30**, 355602 (2019).
- ¹⁶ M. Chirtoc, N. Horny, I. Tavman, A. Turgut, I. Kökey, and M. Omastová, International Journal of Thermal Sciences **62**, 50 (2012).
- ¹⁷ G. Georgousis, C. Pandis, A. Kalamiotis, P. Georgiopoulos, A. Kyritsis, E. Kontou, P. Pissis, M. Micusik, K. Czanikova, J. Kulicek, and M. Omastova, Compos B Eng **68**, 162 (2015).
- ¹⁸ C.W. Nan, R. Birringer, D.R. Clarke, and H. Gleiter, J Appl Phys **81**, 6692 (1997).
- ¹⁹ M.S.S.A. Saraswathi, D. Rana, P. Vijayakumar, S. Alwarappan, and A. Nagendran, New Journal of Chemistry **41**, 14315 (2017).
- ²⁰ M.S. Sri Abirami Saraswathi, D. Rana, K. Divya, S. Alwarappan, and A. Nagendran, New Journal of Chemistry **42**, 15803 (2018).
- ²¹ S.A. Putnam, D.G. Cahill, B.J. Ash, and L.S. Schadler, J Appl Phys **94**, 6785 (2003).
- ²² S. Gomès, A. Assy, and P.O. Chapuis, Physica Status Solidi (A) Applications and Materials Science **212**, 477 (2015).
- ²³ Y.H. Zhao, Z.K. Wu, and S.L. Bai, Int J Heat Mass Transf **101**, 470 (2016).
- ²⁴ M. Hareesha, B. Yogesha, L.L. Naik, and D. Saravanabavan, AIP Conf Proc **2316**, 030016 (2021).
- ²⁵ A. Hammiche, H.M. Pollock, M. Song, and D.J. Hourston, Meas Sci Technol **7**, 142 (1996).

- ²⁶ T. Xu, S. Zhou, F. Jiang, N. Song, L. Shi, and P. Ding, *Compos B Eng* **224**, 109205 (2021).
- ²⁷ L. Jin, P. Wang, W. Cao, N. Song, and P. Ding, *ACS Appl Mater Interfaces* **14**, 1747 (2021).
- ²⁸ W. Sun, E. Guen, G. Hamaoui, A.E. Sachar, F. Alzina, C.M. Sotomayor-Torres, P.O. Chapuis, and S. Gomes, 2020 26th International Workshop on Thermal Investigations of ICs and Systems, THERMINIC 2020 - Proceedings (2020).
- ²⁹ W.P. King, B. Bhatia, J.R. Felts, H.J. Kim, B. Kwon, B. Lee, S. Somnath, and M. Rosenberger, *Annual Review of Heat Transfer* **16**, 287 (2013).
- ³⁰ M. Serhan, M. Sprowls, D. Jackemeyer, M. Long, I.D. Perez, W. Maret, N. Tao, and E. Forzani, *AICHE Annual Meeting, Conference Proceedings 2019-Novem*, 1 (2019).
- ³¹ R.B. Dinwiddie, R.J. Pylkki, and P.E. West, *Thermal Conductivity* **22**, 668 (1994).
- ³² E. Guen, P.-O. Chapuis, R. Rajkumar, P.S. Dobson, G. Mills, J.M.R. Weaver, and S. Gomés, *J Appl Phys* **128**, 235301 (2020).
- ³³ L. David, S. Gomès, and M. Raynaud, *J Phys D Appl Phys* **40**, 4337 (2007).
- ³⁴ A. Assy, *Development of Two Techniques for Thermal Characterization of Materials: Scanning Thermal Microscopy (SThM) and 2 ω Method* (2015).
- ³⁵ T.P. Nguyen, L. Thiery, S. Euphrasie, S. Gomès, B. Hay, and P. Vairac, *Review of Scientific Instruments* **90**, (2019).
- ³⁶ M. Massoud, *Experimental Characterization of Heat Transfer in*

- Nanostructured Silicon-Based Materials* (2016).
- ³⁷ *QUANTIHEAT EUROPEAN PROJECT Prototype Application Note Page 1 | 5 Thermal Reference Samples* (n.d.).
- ³⁸ E. Guen, P.O. Chapuis, N.J. Kaur, P. Klapetek, and S. Gomés, *Appl Phys Lett* **119**, 161602 (2021).
- ³⁹ V. v. Tsukruk, V. v. Gorbunov, and N. Fuchigami, *Thermochim Acta* **395**, 151 (2002).
- ⁴⁰ Y. Zhang, W. Zhu, F. Hui, M. Lanza, T. Borca-Tasciuc, M.M. Rojo, Y. Zhang, W. Zhu, F. Hui, M. Lanza, and M.M. Rojo, *Adv Funct Mater* **30**, 1900892 (2020).
- ⁴¹ K. Kim, J. Chung, G. Hwang, O. Kwon, and J.S. Lee, *ACS Nano* **5**, 8700 (2011).
- ⁴² A.I. Buzin, P. Kamasa, M. Pyda, and B. Wunderlich, *Thermochim Acta* **381**, 9 (2002).
- ⁴³ M. Chirtoc, N. Horny, J.F. Henry, A. Turgut, I. Kökey, I. Tavman, and M. Omastová, *Int J Thermophys* **33**, 2110 (2012).
- ⁴⁴ C.A. Coulson, *Isr J Chem* **11**, 683 (1973).
- ⁴⁵ J. Bian, X.W. Wei, H.L. Lin, L. Wang, and Z.P. Guan, *J Appl Polym Sci* **124**, 3547 (2011).
- ⁴⁶ M.J. Mochane and A.S. Luyt, *Polym Eng Sci* **55**, 1255 (2015).
- ⁴⁷ J. Jacob, G. Ae, and A.K. Bhowmick, *J Mater Sci* **43**, 702 (2008).
- ⁴⁸ M.J. Biercuk, M.C. Llaguno, M. Radosavljevic, J.K. Hyun, A.T. Johnson, and J.E. Fischer, *Appl Phys Lett* **80**, 2767 (2002).

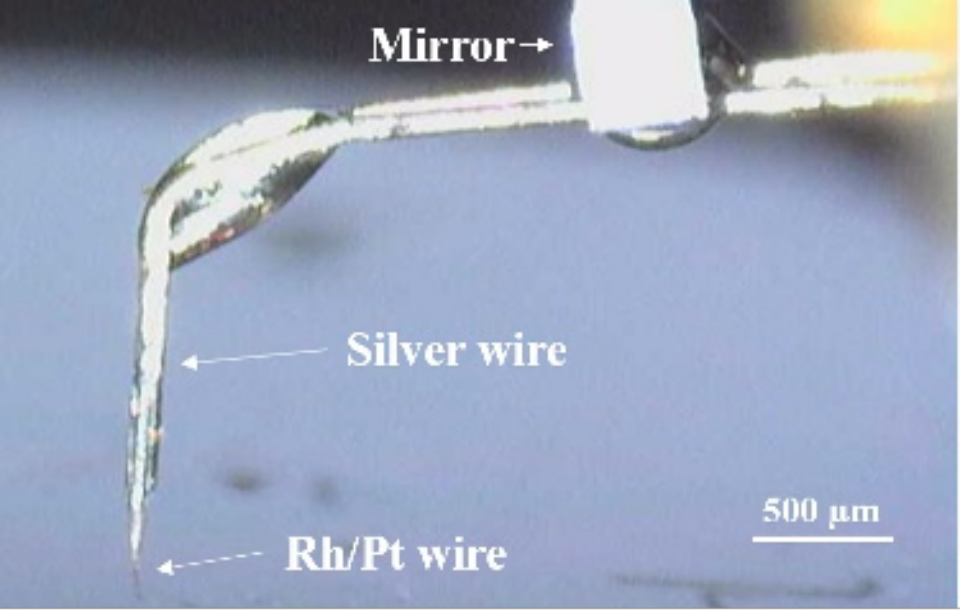
- ⁴⁹ N. Shenogina, S. Shenogin, L. Xue, and P. Keblinski, *Appl Phys Lett* **87**, 1 (2005).
- ⁵⁰ P. Bonnet, D. Sireude, B. Garnier, and O. Chauvet, *Appl Phys Lett* **91**, (2007).
- ⁵¹ J. Yu, R. Qian, and P. Jiang, *Fibers and Polymers* **14**, 1317 (2013).
- ⁵² R. Ram, V. Soni, and D. Khastgir, *Compos B Eng* **185**, 107748 (2020).
- ⁵³ S.K. Karan, A.K. Das, R. Bera, S. Paria, A. Maitra, N.K. Shrivastava, and B.B. Khatua, *RSC Adv* **6**, 37773 (2016).
- ⁵⁴ S.K. Karan, A.K. Das, R. Bera, S. Paria, A. Maitra, N.K. Shrivastava, and B.B. Khatua, *RSC Adv* **6**, 37773 (2016).
- ⁵⁵ H. Pan, B. Na, R. Lv, C. Li, J. Zhu, and Z. Yu, *J Polym Sci B Polym Phys* **50**, 1433 (2012).
- ⁵⁶ R. Gregorio, and M. Cestari, *J Polym Sci B Polym Phys* **32**, 859 (1994).
- ⁵⁷ P. Martins, A.C. Lopes, and S. Lanceros-Mendez, *Prog Polym Sci* **39**, 683 (2014).
- ⁵⁸ L. Ruan, X. Yao, Y. Chang, L. Zhou, G. Qin, and X. Zhang, *Polymers (Basel)* **10**, (2018).
- ⁵⁹ E. Pukada, *IEEE Trans Ultrason Ferroelectr Freq Control* **47**, 1277 (2000).
- ⁶⁰ A. Biswas, K. Henkel, D. Schmeißer, and D. Mandal, *Phase Transitions* **90**, 1205 (2017).

Mirror →

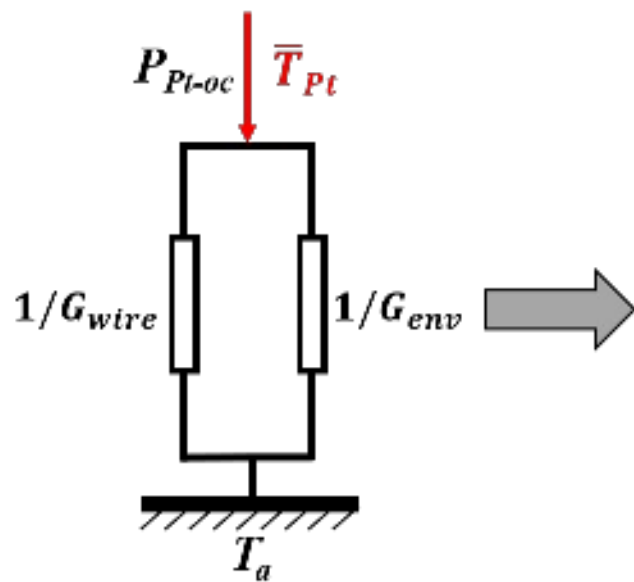
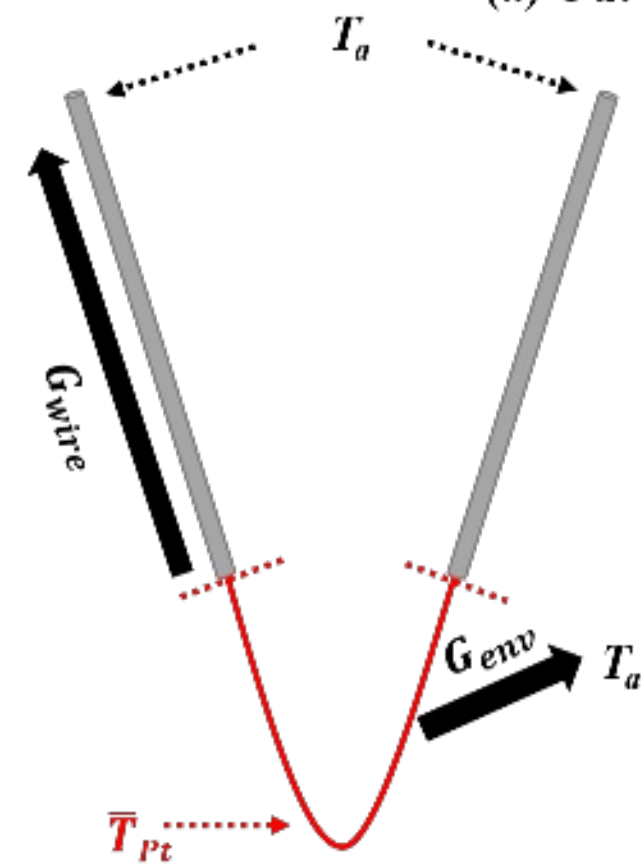
← **Silver wire**

← **Rh/Pt wire**

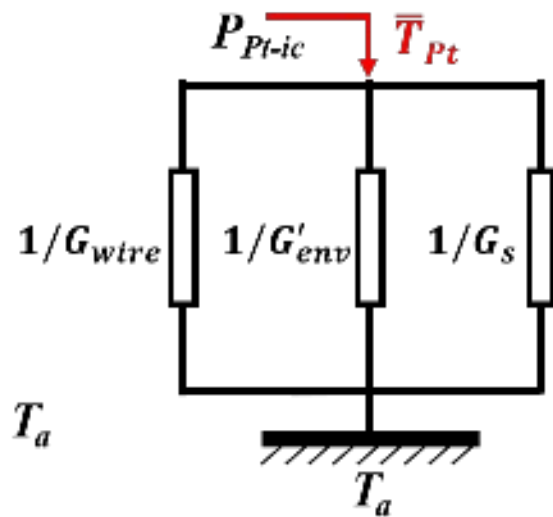
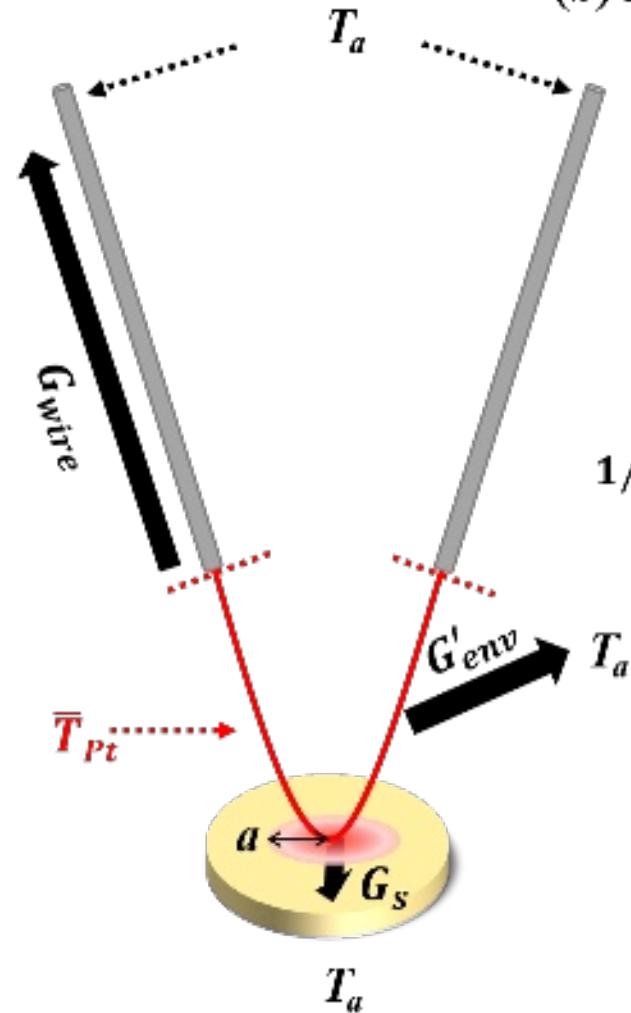
500 μm

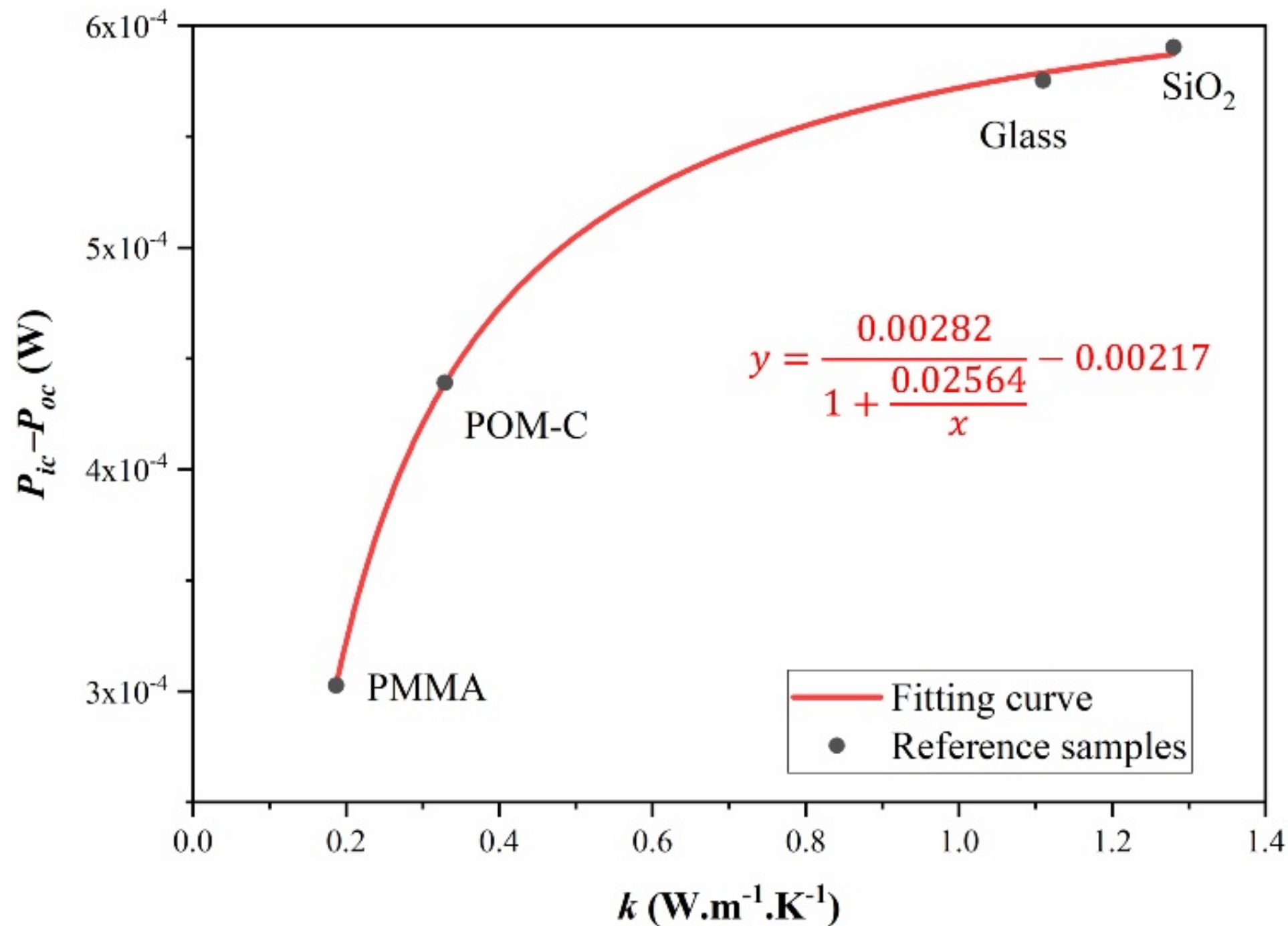
A micrograph showing a thin, metallic wire assembly. The wire is bent into a sharp 90-degree angle. The upper part of the wire is thicker and has a smooth, reflective surface. The lower part is thinner and appears to have a different texture or coating. A scale bar in the bottom right corner indicates a length of 500 micrometers. Labels with arrows point to different parts of the wire: 'Mirror' points to a bright, circular feature at the top right; 'Silver wire' points to the thicker upper section; and 'Rh/Pt wire' points to the thinner lower section.

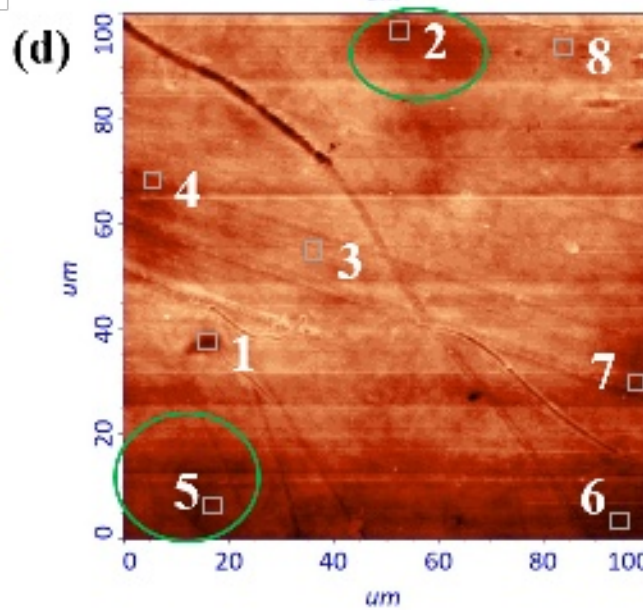
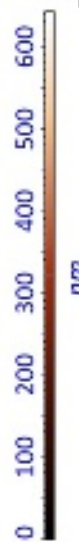
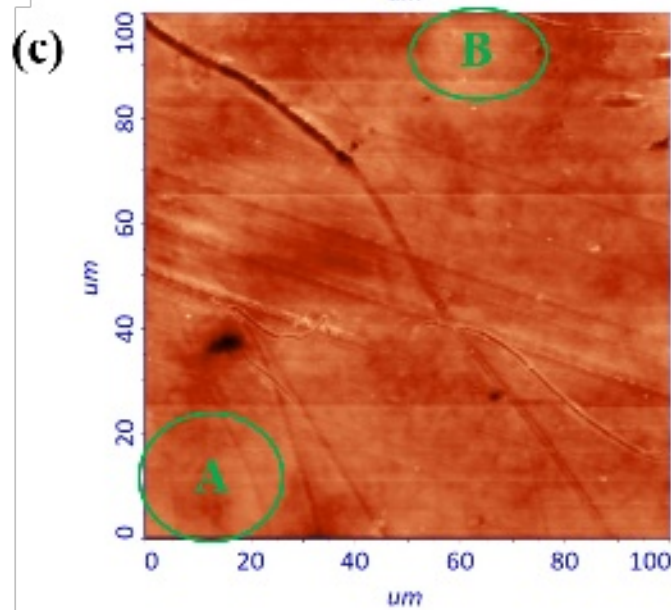
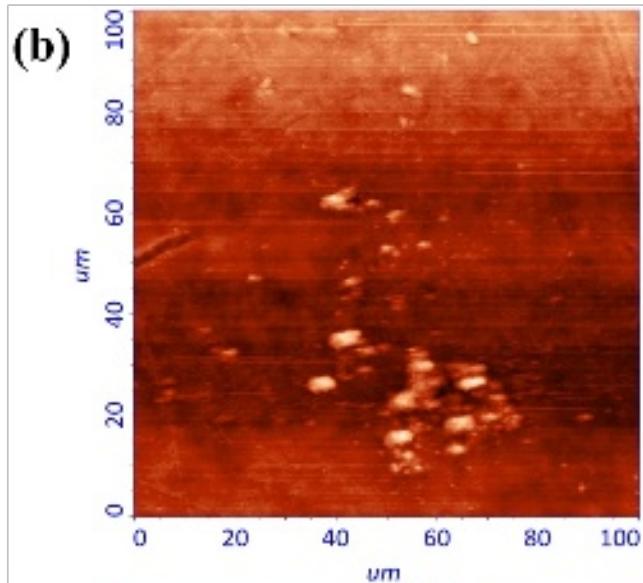
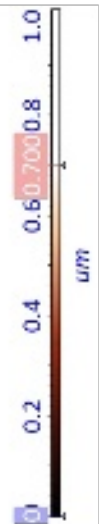
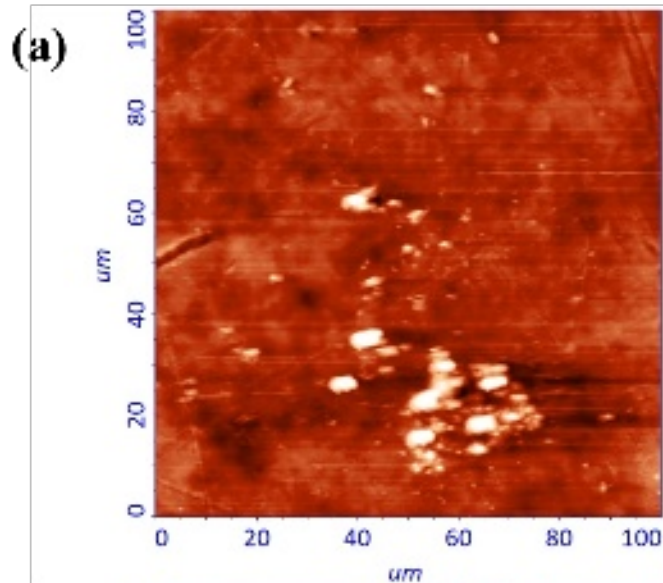
(a) Out of contact

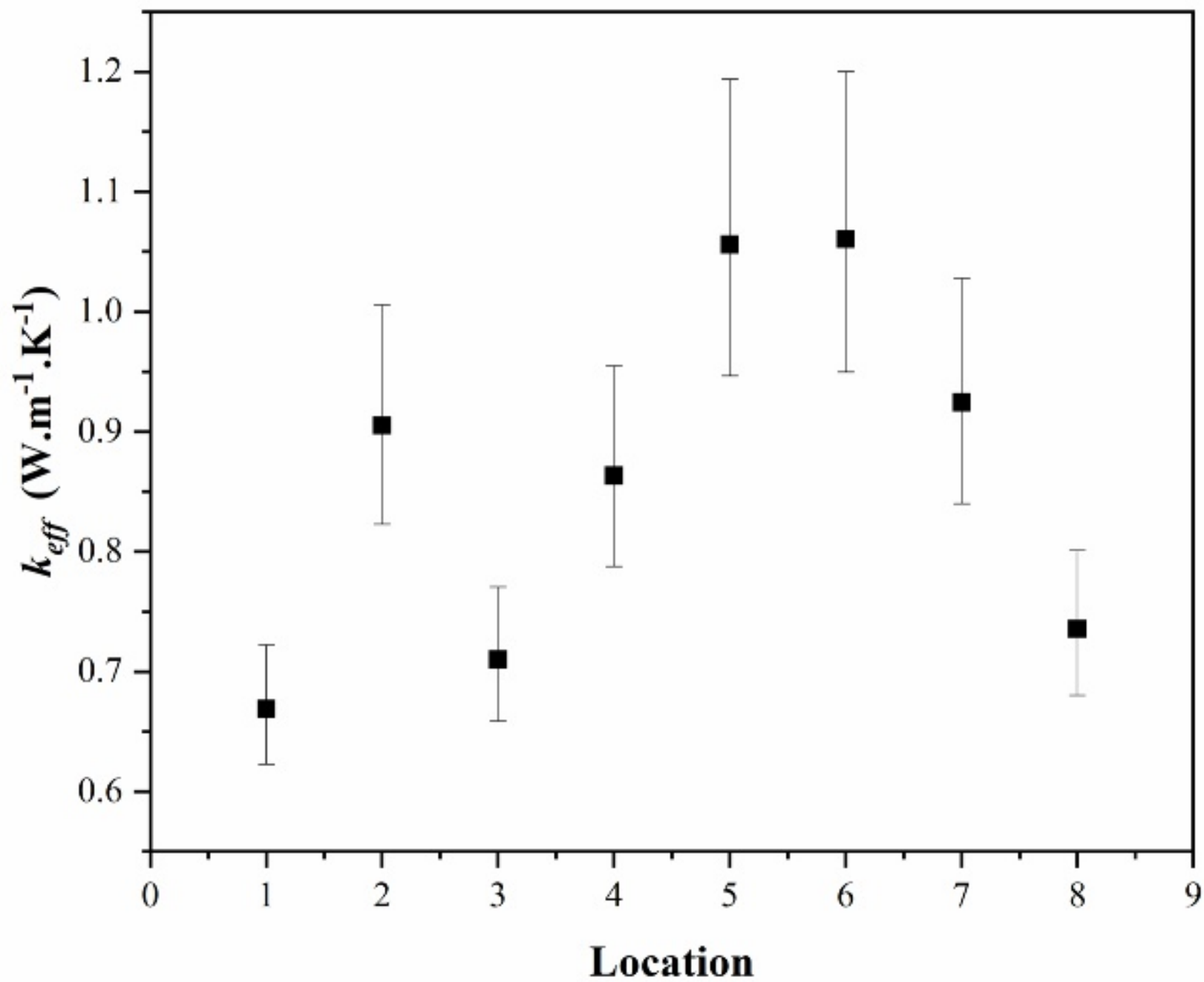


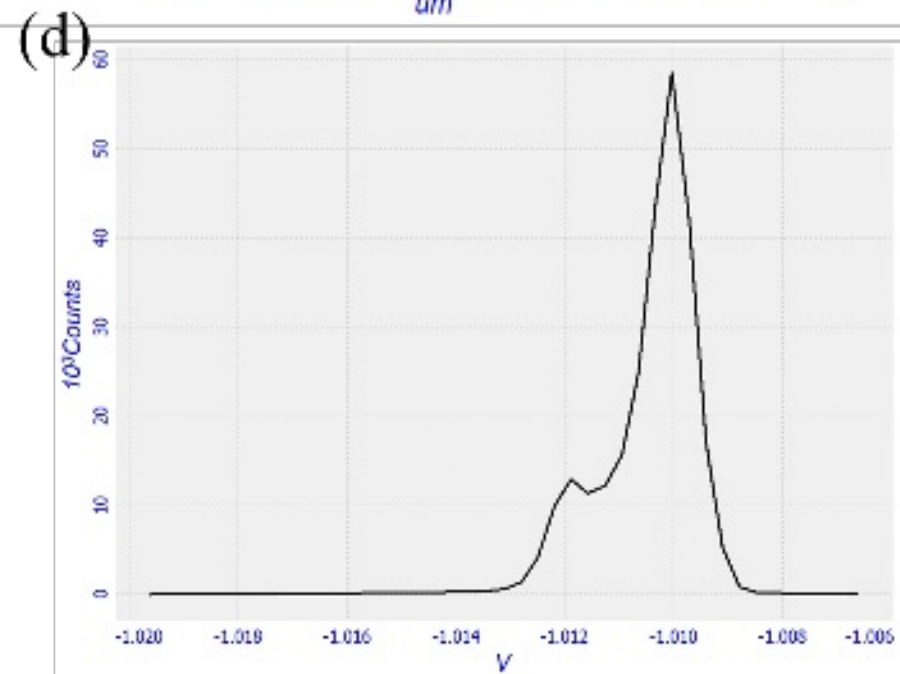
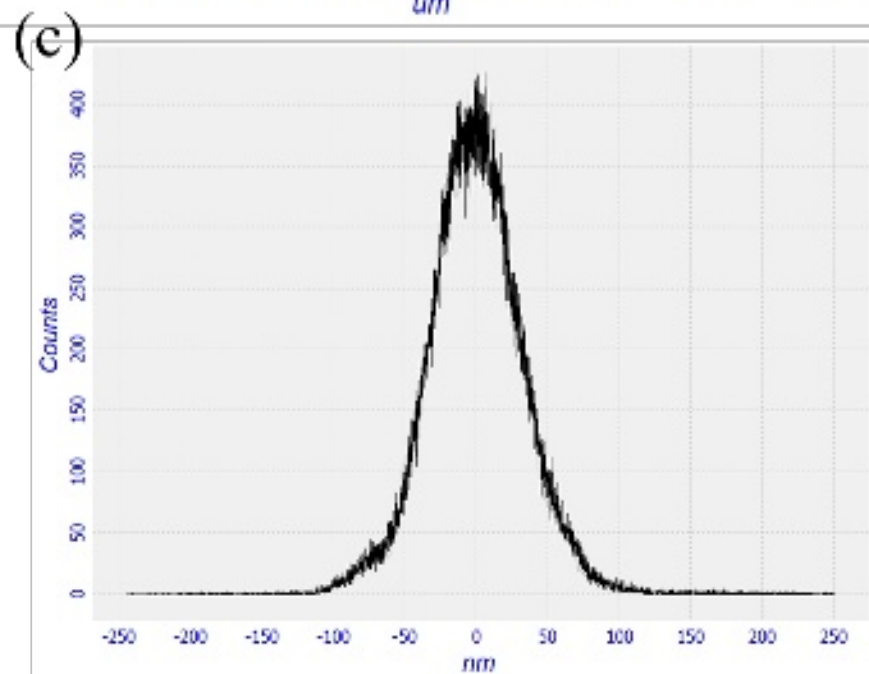
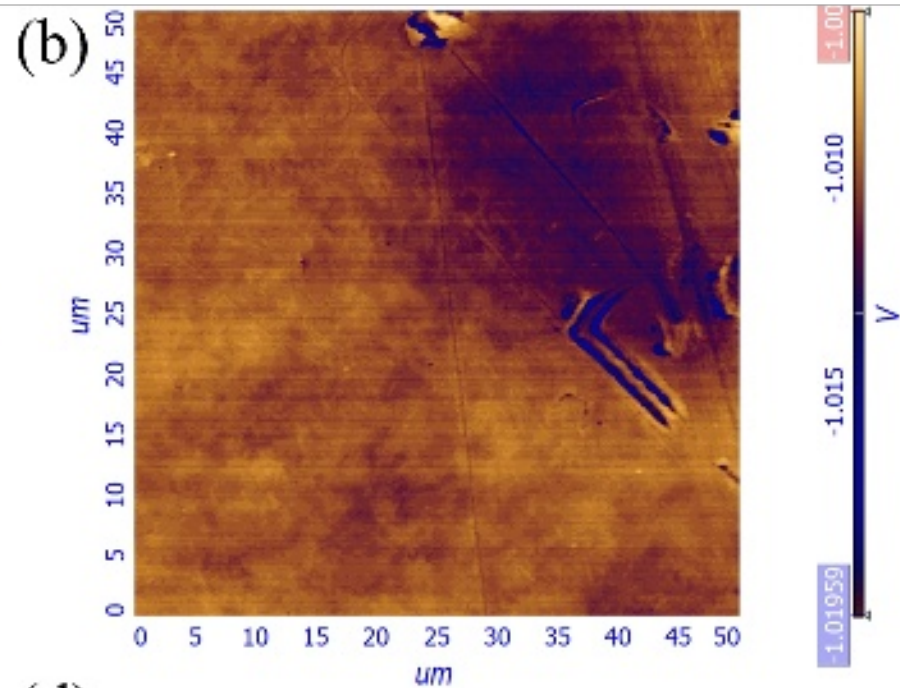
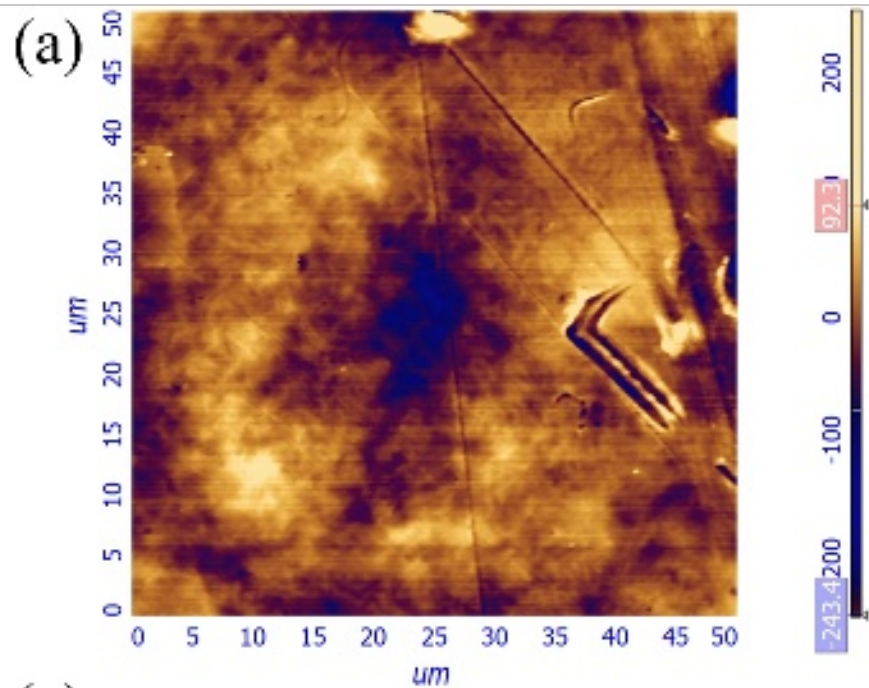
(b) In contact



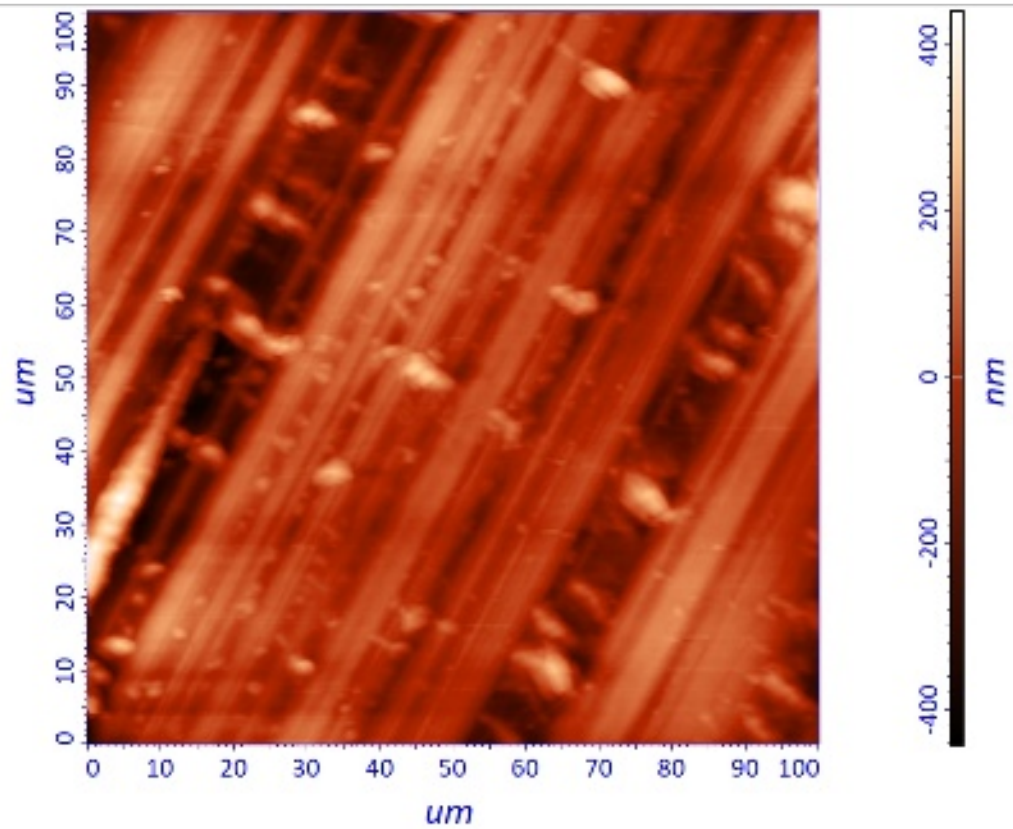








(a) Topography



(b) Thermal image

